Applied Surface Science 540 (2021) 148383

Contents lists available at ScienceDirect

Applied Surface Science

journal homepage: www.elsevier.com/locate/apsusc

# Surface excess free energies and equilibrium Wulff shapes in variable chemical environments at finite temperatures

Mujan N. Seif, Matthew J. Beck *

*Department of Chemical and Materials Engineering, University of Kentucky, Lexington, KY 40506-0046, USA*

ARTICLE INFO

*Keywords:*
Equilibrium Wulff shape
Surface energy
High temperature surface energies
Tungsten

ABSTRACT

Burgeoning interest in nanoparticles across a number of distinct fields has spurred broad investigation into the optimization of particle shape and surface chemistry. Here we demonstrate the application of DFT and DFPT calculations to compute bulk reference free energies and surface excess free energies accounting for vibrational and, where appropriate, configurational entropies of solid particles and particle surfaces. Using these results we construct "particle configuration maps"—graphical maps of the equilibrium shape and surface chemistry of particles over a range of temperatures and environmental conditions. Applied to W particles in O- or Ba/O-containing environments (a model system relevant to thermionic dispenser cathodes with critical applications in vacuum electronic devices) these maps highlight the critical role that Ba plays in controlling both the shape and surface chemistry of W particles in application-relevant conditions. These system-specific findings demonstrate the broad power of DFT+DFPT computed particle configuration maps: revealing connections between and insight into particle behavior and properties as a function of experimentally-relevant conditions.

## 1. Introduction

Proposed applications for nanoparticles are numerous and span seemingly unrelated fields, including drug delivery [1–9], catalysis [10–14], and electron devices [15–19]. In nearly all applications, nanoparticle *shape* is known to have a significant impact on particle properties and behavior [20,21]. Therefore, the ability to predict, or even tailor, particle shape is crucial for improving properties and performance. Both equilibrium particle shape and shape evolution during fabrication are controlled by details of a particle's surfaces—details which are, in turn, controlled by the chemical, thermodynamic, and mechanical conditions or environment in which a particle is found [22–26].

The connections between the conditions in which a particle is found—e.g., chemical environment and/or temperature—and particle shape are complex, as reflected in the diversity of possible surface configurations at the atomic-scale. Here we demonstrate the calculation of temperature- and chemical environment-dependent surface free energies from density functional theory (DFT), and, from these values, the distillation of maps of equilibrium nanoparticle shapes. While the approach described here can be applied to the prediction and optimization of equilibrium nanoparticle shapes generally, in this paper we consider an example system relevant to thermionic, or "hot", cathodes. State-of-the-art Sc-containing ("scandate") cathodes have been shown to exhibit significantly improved performance as compared to related "B-type" cathodes. Both scandate and B-type cathodes consist of pellets of loosely sintered W crystallites (500–1000 nm in diameter) with Ba-containing mixed oxide powders in the pores of the pellet. The addition of Sc (to form a scandate cathode) both enhances performance and results in W crystallites with a highly characteristic shape after annealing at high temperatures (~1150° for on the order of 24 h) [27]. Significant current research is focused on understanding the origin of this characteristic (0 0 1)-, (1 1 0)-, and (1 1 2)-terminated W crystallite shape and the roles that surface composition and annealing temperature play in its stabilization [27–31]. We directly support these studies by examining temperature- and chemical environment-dependent surface free energies and reporting "particle configuration maps" for B-type conditions: particles with bare, O-terminated, and Ba/O-terminated W (0 0 1), (1 1 0), and (1 1 2) surfaces.

As-fabricated nanoparticle shapes are the product of kinetic and thermodynamic factors governing surface configuration and behavior, with kinetics playing a particularly important role in solution processing [22]. For nanoparticles in high-temperature or gas-phase applications, thermodynamic factors increasingly control surface configurations, and

* Corresponding author.
*E-mail address:* m.beck@uky.edu (M.J. Beck).

https://doi.org/10.1016/j.apsusc.2020.148383
Received 18 June 2020; Received in revised form 29 October 2020; Accepted 2 November 2020
Available online 7 November 2020

therefore the stability and evolution of particle shape. Numerous experimental studies have examined the effect of temperature on stable particle shape [32–39]. Though the thermodynamic effects of chemical environment are often challenging to distinguish from kinetic effects, significant recent effort has focused on effects of gas-phase environments on particle shape [40–46], including a subset that have focused on the role of oxygen availability [31,47–58].

Density functional theory (DFT) allows accurate calculation of ground state, or "zero-temperature", atomic-scale structures and energies of possible surface configurations. On their own, these temperature- and environment-independent results can be used to approximate stable particle shapes in qualitatively described chemical environments by treating the reference energies of environmental species as free parameters [45]. Temperature effects due to changes in the chemical environment can be approximated by treating the temperature dependence of these reference energies as that for an ideal gas [57,59]. Measured thermochemical data [60] has been used for the reference energies of gas-phase environmental species allowing improved comparisons to measurable temperatures and chemical environments (via partial pressures). This combination of DFT-calculated properties of the solid and surface plus thermochemical data for the gas-phase environment has been widely used to predict the stability of particular surface configurations [50,56,58,61,62]. Despite the incorporation of temperature-dependent environmental properties, all of these predictions for particle shape and/or surface stability are still limited in that "zero-temperature" DFT calculations of the solid and its surfaces neglect entropic contributions—that is, such calculations do not yield the surface *free energies* that ultimately govern particle shape.

Separately, density functional perturbation theory (DFPT) has been widely applied to compute the properties of phonons from DFT, including the phonon density of states and vibrational contributions to entropy [63–65]. This has allowed direct calculation of both bulk reference *free energies* [61,62] and surface *free energies* [64,66–68]. Calculations of this type are generally limited to a small number of surface configurations, and do not address equilibrium particle shape or chemical effects due to a particle's environment. Recently DFPT has been used to augment thermochemical data (applicable to isolated molecules) by adding a correction for changes in vibrational entropy of environmental species due to surface absorption [67]. In addition, a very recent paper has used DFPT calculated surface free energies to predict the Wulff shape of W in pure vacuum conditions (that is, absent any chemical environment) [68]. In the following we extend these approaches to directly compute temperature- and chemical environment-dependent equilibrium shapes for W particles exposed to O and/or Ba. We also account for the configurational entropy arising from adsorbate diffusion on solid surfaces. This approach allows formulation of maps of equilibrium particle shape under realistic experimental conditions–including those relevant to the optimization and application of W-based thermionic cathodes [27–31].

## 2. Background and methods

### 2.1. Thermodynamic approach

In the thermodynamic limit, a particle will assume the shape that minimizes the total surface excess free energy. This equilibrium shape is called the Wulff shape, and can be deduced, via the Wulff construction, from knowledge of the surface excess free energies of any surface configurations that may appear [22,69]. A "surface configuration" is a specific composition and arrangement of atoms at, near, or on a particular surface. For crystals, surface configurations are first classified by their planar orientation relative to the underlying crystal's principle axes. Facets are regions of appreciable surface area sharing a common, identifiable orientation. Patterns of atoms present at a surface facet may be reconstructions of the underlying bulk structure, have compositions that differ from the bulk, and/or be decorated with atomic or molecular adsorbates. Full determination of the true Wulff shape requires knowledge of the free energies of the non-finite set of all possible surface configurations. In practice, only a small subset of all possible configurations have any meaningful likelihood of being expressed by a real particle: essentially configurations that are minimal, or highly regular, reconstructions of the underlying crystal structure (most likely driven by changes that satisfy broken surface bonds), and/or configurations with environmentally-determined atoms or molecules incorporated or adsorbed at high-symmetry or broken bond sites on the surface.

A key challenge in applying the Wulff construction with DFT-computed surface energies is that, alone, DFT only yields ground-state, zero-temperature energies that do not account for entropy or zero-point vibrational energy [$E_{DFT} \equiv E(T=0)$]. In addition, DFT computed energies characterize particles in a perfect vacuum [$E_{DFT} \equiv E(P=0)$]. More formally, for $\widehat{G}(T,P) = U - T\widehat{S} + PV$, where the hatted notation ($\widehat{x}$) highlights that $x$ depends on temperature:

$$E_{DFT} \equiv G(T=0, P=0) = U$$

Therefore, $E_{DFT}$ values are not *free energies* as required in the Wulff construction.

Free energies require accounting for entropy and zero-point energies. At elevated temperatures the contribution of entropy to the total free energy grows dramatically. At temperatures below a crystal's melting temperature, vibrational entropy ($\widehat{S}_V$) and vibrational zero-point energy ($E_{VZP}$) will be the major components of this contribution [70]. For surfaces where not every equivalent surface site is occupied, we also include configurational entropy ($S_C$) arising from the exchange of positions of surface adsorbates and vacancies. With $E_{DFT}$, we may write:

$$\widehat{G} = E_{DFT} + \widehat{F}_V - TS_C \tag{1}$$

Here, the combination of DFPT-computed vibrational entropy and zero-point energy takes the form of a Helmholz free energy (where $\widehat{F}_V = E_{VZP} - T\widehat{S}_V$). $S_C$ is computed according to $S_C = k_B \ln \Omega_C$, where $\Omega_C$ counts the number of arrangements of vacant and occupied surface adsorption sites for a given surface configuration, and $S_C$ is normalized by the slab area. This term is zero for surfaces where all equivalent surface sites are occupied and for bulk systems.

Surface excess free energies as a function of temperature ($\widehat{\gamma}$) are then simply the excess free energy present in a system containing a surface, relative to the energy of all species in their (bulk) reference state. In the present calculations, double-sided semi-infinite slabs are used to represent surface facets. The surface free energy per unit area ($\widehat{\gamma}_\alpha$) of a particular surface configuration ($\alpha$), containing $n_i$ atoms of various species $i$, each having reference energy $\widehat{\mu}_i$, is thus:

$$\widehat{G}_{\text{slab},\alpha} = \sum_i \widehat{\mu}_i n_i + 2A_\alpha \widehat{\gamma}_\alpha \tag{2}$$

The factor of two is included to account for the two sides of the slab, each with an area $A_\alpha$. $\widehat{\mu}_i$ is the chemical potential (Gibbs free energy per atom) of the each species $i$ in its reference state. Combining with Eq. 1:

$$\begin{aligned}\widehat{G}_{slab,\alpha} &= E_{DFT,\alpha} + E_{VZP,\alpha} - T(\widehat{S}_{V,\alpha} + S_{C,\alpha}) \\ &= \sum \widehat{\mu}_i N_i + 2A_\alpha \widehat{\gamma}_\alpha\end{aligned} \tag{3}$$

Or:

$$\widehat{\gamma}_\alpha = \frac{E_{DFT,\alpha} + E_{VZP,\alpha} - T\left(\widehat{S}_{V,\alpha} + S_{C,\alpha}\right) - \sum \widehat{\mu}_i N_i}{2A_\alpha} \tag{4}$$

Finally, the equilibrium particle shape, or Wulff shape, is that which minimizes the total surface excess energy ($\widehat{\Gamma}$) at fixed volume, where:

$$\widehat{\Gamma} = \sum_\alpha \widehat{\gamma}_\alpha A_\alpha \tag{5}$$

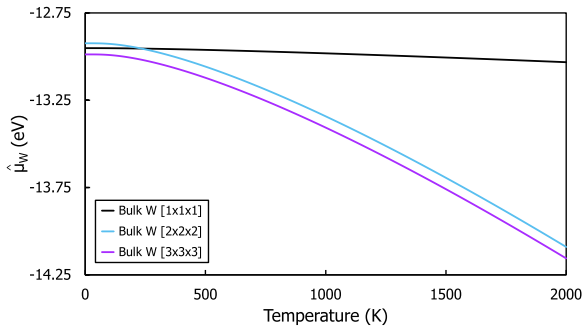


**Fig. 1.** $\widehat{\mu}_W$ as a function of temperature for three bulk supercells.

The Wulff construction [71] is the geometrical equivalent of Eq. 5, where $\widehat{\Gamma}$ is minimized for the convex hull of all surface configurations, $\alpha$, each constructed a distance proportional to $\widehat{\gamma}_\alpha$ from the origin. That is, $\widehat{\Gamma}$ is minimized for the smallest closed shape formed from planes representing each surface configuration arranged with $h_\alpha = \lambda\widehat{\gamma}_\alpha$ for $h_\alpha$, the height along the plane normal from the origin for each surface configuration $\alpha$, and $\lambda$, a scaling factor.

### 2.2. Calculation details

In the following, the commercial planewave pseudopotential code, VASP (Vienna *Ab initio* Simulation Package) [72], was used for all DFT calculations. Pseudopotentials based on the Perdew-Burke-Ernzerhof (PBE) formalism of the generalized gradient approximation (GGA) [73] with projector augmented wave method (PAW) [74] were used for all atoms. The W ($5p^6 6s^2 5d^4$), Ba ($5s^6 5p^6 6s^2$), and O ($2s^2 2p^4$) electrons were included in the respective valences. Brillouin zone sampling was done with Monkhorst-Pack $k$-point meshes with densities at least 30 $k$-points/$A^{-1}$ in each direction for each calculation. Atomic positions were relaxed according to calculated interatomic forces until the total energy was converged to better than $1 \times 10^{-7}$ eV/atom. The planewave expansion of the wavefunction was truncated at 520 eV.

For the bulk systems relevant to this study—W, $WO_3$, Ba, and BaO—reference energies were determined by converging $\widehat{\mu}_i$ with respect to system size. Supercells ranging in size up to $3 \times 3 \times 3, 2 \times 2 \times 2, 3 \times 3 \times 3$, and $2 \times 2 \times 2$ bulk unit cells were considered for W, $WO_3$, Ba, and BaO respectively. Bulk $\widehat{\mu}_i(T)$ curves for each of these species can be found in the Appendix. (0 0 1), (1 1 0), and (1 1 2) surfaces were considered based on previous characterization results for scandate cathodes, and were represented as periodic semi-infinite W slabs with thicknesses of 13, 9, and 19 atomic layers (~20.6 Å, ~19.12 Å, and ~23.4 Å of W, respectively). Slabs were separated by a minimum vacuum spacing of 32–40 Å. For each surface, the W slab was left bare or decorated with various configurations of adsorbed O or Ba and O atoms, following Zhou et al. [31]. In addition, the [2 × 2] reconstructed and [2 × 2] supercell of ideal-terminated W (0 0 1) surfaces were both considered [68,75], as was a newly identified [2 × 2] "zig-zag" reconstruction of the Ba and O-decorated (1 1 2) surface (see Fig. 8 in the Appendix). For images and details of all surface configurations except the bare W [2 × 2] (0 0 1) and the zig-zag Ba/O [2 × 2] W (1 1 2) see Ref. [31].

$\widehat{F}_V$ and $E_{VZP}$ were calculated using PHONOPY, an open source software package that leverages VASP for DFPT calculations [63]. Phonon properties were calculated in the harmonic approximation, and were computed separately for bulk and surface slab systems. The software package Wulffmaker [69], which implements the Wulff construction in a user-friendly interface, was used to draw representations of the Wulff shape for selected sets of calculated $\widehat{\gamma}_\alpha$ values.

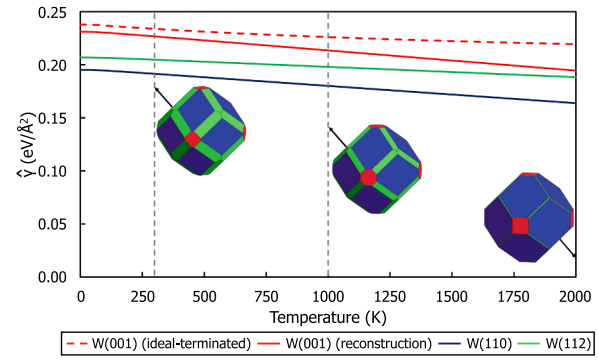


**Fig. 2.** Surface energies and correlated equilibrium Wulff shapes of bare W surfaces at three temperatures: 300 K, 1000 K, 2000 K.

## 3. Results and discussion

### 3.1. W particle shapes in pure vacuum

To compute the surface free energies required to determine the Wulff shape, temperature-dependent bulk reference free energies were required. While single primitive cells are sufficient to resolve zero-temperature, ground-state properties of bulk crystals, free energies accounting for vibrational entropy require supercells large enough to capture the set of activated phonons. Fig. 1 shows computed bulk free energies per atom of W (from Eq. 1) for different supercells as a function of temperature. Cubic bulk W supercells of various sizes were studied to determine convergence of $\widehat{F}_V$ with respect to volume. As can be seen in Fig. 1, the primitive W unit cell significantly underestimates the contribution of $\widehat{S}_V$, leading to a nominally constant $\widehat{\mu}_W$, even at elevated temperatures. The largest supercell (3 × 3 × 3) was selected as the converged $\widehat{\mu}_W$ and this curve was used as the W reference for all computed surface energies. Similar $N \times N \times N$ supercells were used to compute $\widehat{\mu}_i$ values for of $WO_3$, Ba, and BaO. $2 \times 2 \times 2, 3 \times 3 \times 3$, and $2 \times 2 \times 2$ supercells were selected as converged references for these species, respectively, and are reported as a function of temperature in Fig. 7 of the Appendix.

Surface free energies as a function of temperature for bare W (0 0 1), (1 1 0), and (1 1 2) (that is, W in a pure vacuum) are shown in Fig. 2, as well as a selection of resulting Wulff shapes at 300, 1000, and 2000 K. These surface energies do not include a configurational entropy term, since uniform terminations with no vacancies are expected on bare metal surfaces. At all temperatures, the surface free energy of W (1 1 0) is lower than that of the both W (0 0 1) and W (1 1 2) surfaces, and, consistent with previous experiment [76–81] and calculation [68,82], W particle shapes are found to be dominated by (1 1 0) surfaces. Considering bare W (0 0 1) in isolation, the [2 × 2] reconstructed surface has the lowest free energy at all temperatures. At 0 K, the reconstructed W (0 0 1) surface is 6.82 meV lower than the ideal-terminated configuration, similar to the 6.87 meV (0.11 J/m$^2$) lower energy reported in Ref. [68]. The bare W (1 1 2) has lower surface excess energy than bare W (0 0 1) at all considered temperatures, and at temperatures below ~1000 K the W (1 1 2) has low enough surface energy that it would be expected to appear on particles exhibiting the equilibrium shape. At these temperatures achieving the equilibrium shape may be kinetically constrained, though increasing "rounding" of (1 1 0)/(1 1 0) edges due to the appearance of (1 1 2) facets should be expected. At all temperatures corners at the intersection of three (1 1 0)-type planes should be expected to be truncated with small (0 0 1) facets.

### 3.2. W particles in an Ba/O-containing environment

We now consider the equilibrium shape of W particles in a chemical environment containing O, or Ba and O, and specifically the equilibrium

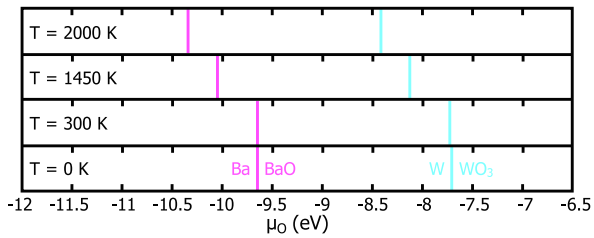


**Fig. 3.** The regions of stability for a metal and its respective oxide as a function of temperature for W and Ba.

W particle shape as a function of both temperature and $O_2$ partial pressure. The Ba/O-on-W system is highly relevant for thermionic ("hot") dispenser cathodes with critical applications in vacuum electronics [27–31]. Cathodes consist of loosely sintered pellets of micron or sub-micron W crystallites, and are heated to high temperature (>1000 K) to initiate thermionic electron emission. Extensive studies have shown that Ba cations adsorbed atop O-terminated W surfaces in so-called B-type cathodes dramatically enhance thermionic emission [28,31,83]. In addition, recent studies have shown that B-type cathodes can be further enhanced with the addition of Sc. These scandate cathodes exhibit extremely high emitted current densities, and also a characteristic (0 0 1)-, (1 1 0)-, (1 1 2)-terminated shape, highlighting a direct connection between equilibrium shape and device performance during operation [27].

Experiment has shown that while O is present during cathode operation, its availability is not sufficient to oxidize W particles to $WO_3$, even after annealing at elevated temperature (1300 K and higher) for 100s or 1000s of hours [27]. In addition, both BaO and metallic Ba are observed to be present inside the sealed environments in which cathodes operate, implying enough O is available to oxidize at least a significant fraction of available Ba [84]. These observations of the presence of certain bulk phases represent limits on the chemical potential of O in the W particle's environment.

For a general oxidation reaction at equilibrium, when a bulk metal $M$ is in equilibrium with its oxide $MO_X$, we have:

$$\widehat{\mu}_M + X\mu_O = \widehat{\mu}_{MO_X} \tag{6}$$

$$\text{or } \mu_O = \frac{\widehat{\mu}_{MO_X} - \widehat{\mu}_M}{X}$$

When either the metal or the oxide are favored, these become inequalities, with $\widehat{\mu}_M + X\mu_O$ lower when the metal is stable, and $\widehat{\mu}_{MO_X}$ lower when the oxide is favored. For a Ba/O/W containing system relevant to cathodes, where both metallic W and Ba oxide are present, we have for W $\widehat{\mu}_W + 3\mu_O < \widehat{\mu}_{WO_3}$, and for Ba, $\widehat{\mu}_{Ba} + \mu_O \geqslant \widehat{\mu}_{BaO}$. Rearranging, this gives limits on the value of $\widehat{\mu}_O$ implied by experiment:

$$\mu_O < \frac{\widehat{\mu}_{WO_3} - \widehat{\mu}_W}{3}$$

$$\text{and } \mu_O \geqslant \widehat{\mu}_{BaO} - \widehat{\mu}_{Ba}$$

Fig. 3 shows these limits on $\mu_O$—effective the equilibrium phase boundaries between W/$WO_3$ and Ba/BaO—at 0, 300, 1450, and 2000 K, as derived for computed bulk free energies (chemical potentials) of W (from above), $WO_3$, Ba, and BaO (see Fig. 7 in the Appendix).

To study W particle shapes relevant in cathode environments, the properties of various Ba/O-on-W surface configurations were computed: $Ba_{0.50}$O-*top*/W(0 0 1), $Ba_{0.25}$O-*tri*/W(1 1 0), $Ba_{0.50}$O-*top*/W(1 1 2) ([2 × 1] row and [2 × 2] zig-zag), O-*top*/W(0 0 1), O-*top*/W(1 1 0), O-*top*/W(1 1 2), bare W(0 0 1) (ideal-terminated and [2 × 2] reconstructed), bare W(1 1 0), and bare W(1 1 2). These surfaces were considered because they represent the collection of thermodynamically-stable, lowest surface energy configurations as determined in previous zero-temperature calculations by Zhou et al. [31] for W particles in environments containing Ba and O.

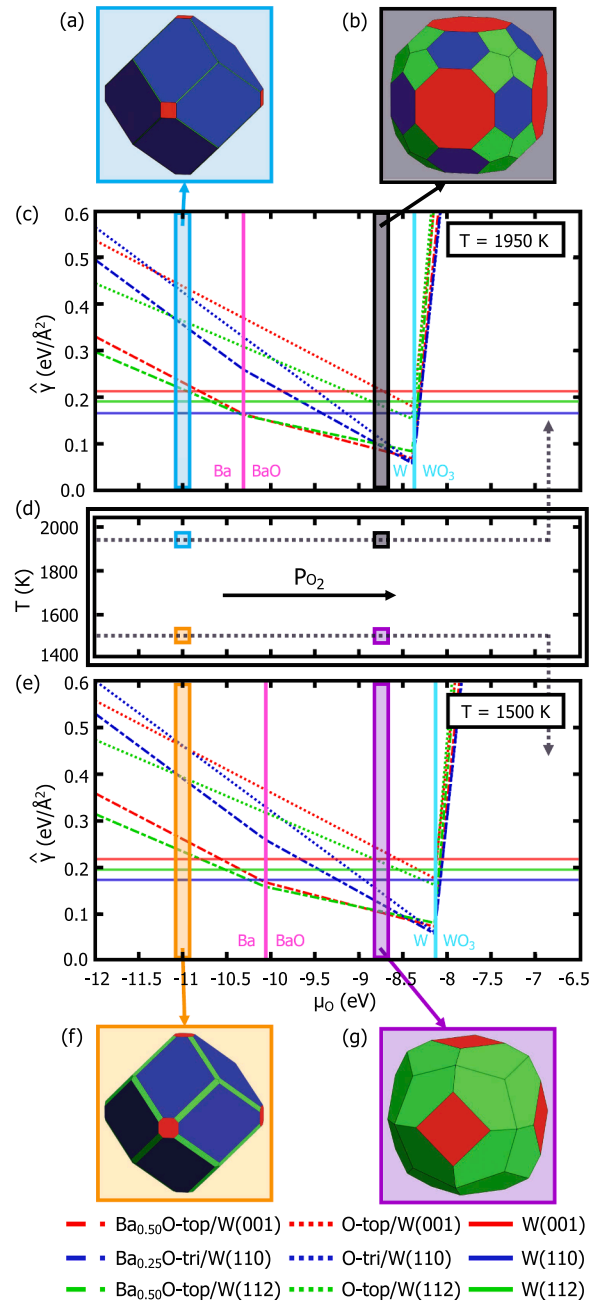


**Fig. 4.** Four combinations of $P_{O_2}$ and $T$ are highlighted in (d). These pairs are extended to (c) and (e), which show $\widehat{\gamma}$ as a function of $\mu_O$ at two temperatures: 1500 K and 1950 K. The minimum $\widehat{\gamma}$ surfaces were used to construct four Wulff shapes, each exhibiting varying degrees of (0 0 1), (1 1 0), and (1 1 2) facets, highlighting the critical dependence of $\widehat{\gamma}$ on both $T$ and $\mu_O$. Figures (a) and (f) are both comprised only of bare W facets, and appear quite similar except for the slight appearance of (1 1 2) in Fig. (f). Figure (b) prominently exhibits all three facets, and is comprised of the $Ba_{0.50}$O-*top*/W(0 0 1), $Ba_{0.25}$O-*tri*/W(1 1 0), and is the $Ba_{0.50}$O-*top*/W(1 1 2) configurations. Figure (g) does not exhibit the (1 1 0) facet, only including the $Ba_{0.50}$O-*top*/W(0 0 1) and $Ba_{0.50}$O-*top*/W(1 1 2) configurations. At both of these temperatures, bare W(0 0 1) refers to the reconstruction.

We have computed $\widehat{F}_V$ and $S_C$ values for each of these surfaces, which, when combined with the temperature-dependent bulk chemical potentials already discussed, allow determination of fully temperature- and chemical environment-dependent surface excess free energies. In computing $\widehat{F}_V$, phonon density of states (pDOS) were required for both

bulk and slab systems. Plots of pDOS for the nine Ba/O-on-W surfaces are presented in the Appendix (Fig. 9). Analysis of the pDOS for surface slabs provides a test of the structural stability of the surface configurations considered beyond relaxation of structures according to their interatomic forces, as stable structures are local energy minima, and therefore have no imaginary phonon modes. DFPT calculations of structures relaxed according to their interatomic forces until total energies were converged within $1 \times 10^{-7}$ eV/atom show there are no imaginary phonon modes for any of the bare W, O-on-W, or Ba/O-on-W surfaces except (i) the ideal-terminated bare W (0 0 1) and (ii) the $Ba_{0.50}$O-*top*/W(1 1 2) surface.

In the case of ideal-terminated W (0 0 1), imaginary modes with frequencies ranging from $6.0 \times 10^9$ to $2.3 \times 10^{12}$ Hz simply reflect that the [2 × 2] reconstruction, rather than the ideal-terminated surface, is stable, and the (relaxed) reconstructed surface is found to have no imaginary modes. The case of $Ba_{0.50}$O-*top*/W(1 1 2) is more complicated, with the (relaxed) [2 × 1] "row" reconstruction reported by Zhou et al. [31] found to exhibit a single imaginary mode with a frequency of $8.55 \times 10^8$ Hz. The Ba atoms in this surface are in alternating rows, and the imaginary mode involves an in-plane shift by the surface Ba towards a neighboring (unoccupied) surface site. Further analysis of up to [4 × 2] $Ba_{0.50}$O-*top*/W(1 1 2) surfaces shows that a [2 × 2] "zig-zag" pattern of Ba atoms yields a reconstruction with slightly lower energy (by ~1 eV/Å$^2$), but that also exhibits a low frequency imaginary mode ($2.32 \times 10^{10}$ Hz).

Despite DFPT finding this mode to be imaginary (indicating that the surface configuration is not a local minimum), direct, discrete calculation of the energy of the $Ba_{0.50}$O-*top*/W(1 1 2) "zig-zag" with displacements (of varying magnitude) in the hyperdirection of this mode find the relaxed structure to be the lowest in energy. Based on the facts that both [2 × 1] and [2 × 2] "zig-zag" structures are relaxed structures, that both imaginary modes are relatively low frequency (implying a slowly varying potential energy surface), and that direct calculation of the energy of relaxed "zig-zag" structures displaced according to the imaginary mode confirm a minimum energy configuration, we hypothesize that the arrangement of Ba atoms on the O-covered W (1 1 2) is not unique (at least at any finite temperature), instead sampling a range of close-lying energy minima (e.g. combinations of "row" and "zig-zag" configurations), suggesting significant disorder in Ba arrangement on this surface, and possibly fast Ba surface diffusion. Further examination of the kinetics of this surface are warranted, but beyond the scope of this study. In computing equilibrium crystal shapes we have chosen to use the low-energy [2 × 2] "zig-zag" structure, though the similar energetics (both zero temperature $E_{DFT}$ and temperature-dependent $\widehat{F}_V$ are within ~1% of each other) of the [2 × 2] and [2 × 1] yield qualitatively indistinguishable equilibrium shapes.

Combining all computed bulk and surface free energies, Fig. 4 summarizes the effects of varying temperature and $\mu_O$ by showing equilibrium W crystal shapes [Figs. 4] at $T = 1950$ and 1500 K and $\mu_O = -11$ and $-8.75$ eV. Figs. 4(c) and (e) show the $\mu_O$-dependent surface energies at the two temperatures, and Fig. 4(d) indicates the relative positions of the selected $(T, \mu_O)$ points in phase space. Surface free energies for the nine surface configurations [$\widehat{\gamma}_\alpha(\mu_O)$] are shown as red, green, and blue curves in Figs. 4(c) and (e). Fig. 4(c) shows surface free energies at 1950 K, and Fig. 4(e) at 1500 K. Red curves correspond to (0 0 1) surface configurations, blue curves to (1 1 0) configurations, and green curves to (1 1 2) configurations. At both of these temperatures, $Ba_{0.50}$O-*top*/W(1 1 2) [2 × 2] and [2 × 1] exhibit comparable surface excess free energies, and are thus not distinguished in this discussion. The W (0 0 1) curve is for the [2 × 2] reconstruction. The M/$MO_X$ equilibrium values of $\mu_O$ are shown as the solid magenta (Ba/BaO) and cyan (W/$WO_3$) vertical bars. The $\widehat{\gamma}_\alpha(\mu_O)$ curves are discontinuous at these bulk phase boundaries, as would be expected based on an examination of Eq. 4.

Fig. 4(d) shows a diagram akin to a temperature–pressure phase diagram. Oxygen partial pressure is represented by $\mu_O$, the O chemical potential, or, equivalently, the chemical availability of O in the system. Selecting two $\mu_O$ points in each of the 1500 K and 1950 K plots of $\widehat{\gamma}_\alpha(\mu_O)$ [blue/orange and gray/purple vertical highlights in Fig. 4(c) and (e)] is equivalent to selecting four distinct $(T, \mu_O)$ points on the temperature–pressure diagram, Fig. 4(c). Figs. 4 (a), (b), (f) and (g) show the different equilibrium shapes of W particles at the four different $(T, \mu_O)$ points.

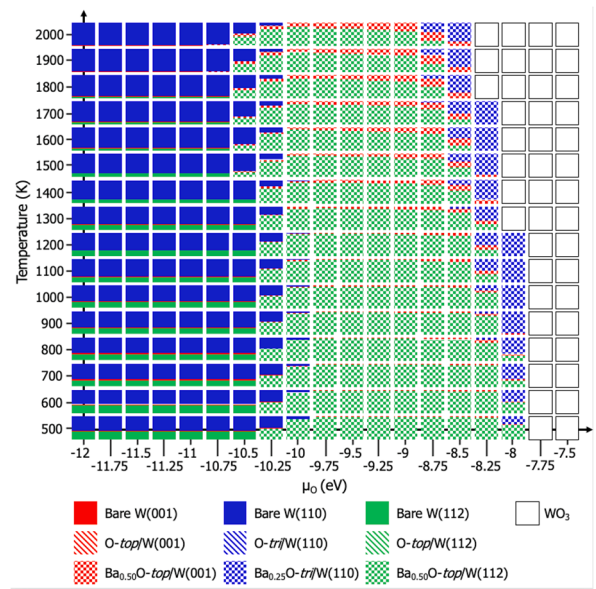


**Fig. 5.** Prominent surface facets for W nanoparticles as a function of temperature, $\mu_O$, and adsorbed Ba/O species. $WO_3$ exists at all temperatures given a $\mu_O >$ ~-8.25 eV. At low $\mu_O$ and high $\mu_O$ (before it fully oxides to $WO_3$) the nanoparticle is predominantly (1 1 0) terminated. At low $\mu_O$, the surface is bare; at high $\mu_O$, the surface is Ba-O-terminated. At moderate $\mu_O$, the nanoparticle is dominated by the (1 1 2) facet. With the addition of Ba to the O-W system, there is no $\mu_O$ or temperature wherein a O-terminated configuration is featured on the nanoparticle.

It should be noted that the values of $\widehat{\gamma}_\alpha$ represent a set of surfaces in $(T, \mu_O)$ space. Fig. 4 shows isothermal sections of the full 3D data set, with each $\widehat{\gamma}_\alpha$ surface appearing as a curve. Movies showing the evolution of similar isothermal sections of $\widehat{\gamma}_\alpha(\mu_O)$ curves as temperature varies are available elsewhere [85].

In addition, the contribution to the surface free energy from vibrational entropy is consistently far more significant than from configurational entropy, though this varies significantly as temperature varies. For example, for the $Ba_{0.50}$O-*top*/W(0 0 1), at 100 K, vibrational entropy is calculated to be 516× greater than configurational entropy; at 2000 K, this ratio increases to 6542× (vibrational entropy remaining greater). Excluding configurational entropy would have a relatively minor effect on the conclusions drawn from the present results.

The equilibrium particle shape (Wulff shape) at any particular values of $T = T^*$ and $\mu_O = \mu_O^*$ can are determined by carrying out the Wulff construction with the set of $\widehat{\gamma}_\alpha(T^*, \mu_O^*)$ values. The Wulff construction yields not only the equilibrium shape, but also information as to the specific surface configurations (orientation, composition, and surface atom arrangement) that are expressed by W particles at the given conditions. Therefore, the content of Fig. 4 can be expanded into a "particle configuration map" indicating both the shape of W particles and the details of the chemistry of the particles' surfaces at every temperature and $\mu_O$.

Fig. 5 is a particle configuration map for W particles in a Ba/O-containing environment as a function of $\mu_O$. Each box represents a point in $(T, \mu_O)$ space, with the box's color and style indicating the presence of particular surface configurations in the Wulff shape. Red,

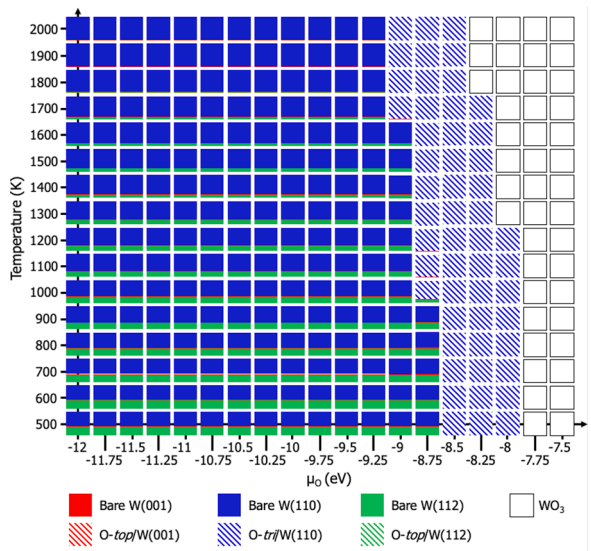


**Fig. 6.** Prominent surface facets for W nanoparticles as a function of temperature, $\mu_O$, and adsorbed O species. $WO_3$ exists at almost all temperatures given a $\mu_O$ >-7.75 eV. While the nanoparticles are terminated with the (1 1 0) facet at almost all temperatures and $\mu_O$, the facet is O-terminated given a $\mu_O$ from −9.5–−8.75 eV, depending on the temperature.

blue, and green again represent (0 0 1), (1 1 0), and (1 1 2) facets, respectively, and solid, hatched, and checked boxes represent bare, O-terminated, and Ba/O-terminated surface configurations, respectively. The area of a particular color and style within a box (representing a particular surface configuration) corresponds to the fraction of particle surface area expressed by the surface configuration at equilibrium. For example, if a box is 60% solid blue and 40% solid red, particles under the correlating conditions would have surface areas comprised of 60% W(1 1 0) and 40% W(0 0 1). Empty white boxes indicate conditions under wherein W particle will oxidize to form $WO_3$.

Examining Fig. 5, it can be seen that at low $O_2$ partial pressure (most negative $\mu_O$), bare W surfaces (solid color boxes) are preferred, with (1 1 0) dominating at all temperatures. This is fully consistent with results for W particles in vacuum, as discussed above, and the fact that strongly negative $\mu_O$ implies extremely low availability (low partial pressures) of O (or $O_2$). As $\mu_O$ increases, that is, as the partial pressure of $O_2$ increases, Ba/O-terminated facets begin to appear at all temperatures. Once $\mu_O$ reaches ~-10.25 eV, depending on $T$, W particles have (i) completely changed shape from principally (1 1 0)-terminated to primarily (1 1 2)-terminated [with some (0 0 1) appearing at elevated temperatures], and (ii) have changed from bare W to Ba/O-terminated. At sufficiently high $\mu_O$, as the bulk W/$WO_3$ phase boundary is approached, both Ba/O-terminated (0 0 1) and (1 1 2) facets disappear, replaced by Ba/O-terminated (1 1 0) facets.

Intriguingly, O-terminated facets never have sufficiently low surface energy to appear with appreciable area on W particles in environments containing both Ba and O. The present results, though, allow construction of a similar particle configuration map to Fig. 5, but for environments where Ba is absent—that is environments containing only O. This is accomplished by including only bare and O-terminated surfaces in the Wulff construction. Fig. 6 is a particle configuration map for W particles in O-only environments as a function of temperature and $\mu_O$. Colors and box styles are the same as in Fig. 5.

Comparison of Figs. 5 and 6 makes immediately clear that the addition of Ba dramatically changes the shape and chemistry of W particle surfaces. In the absence of Ba, W nanoparticles are either (1 1 0) O-terminated, or, below a minimum $\widehat{\mu}_O$, (1 1 0) bare W-terminated, with some bare (0 0 1) or (1 1 2) present. The addition of Ba suppresses the appearance of bare W-terminated particles to more O-poor environments, introducing a wide range of $\widehat{\mu}_O$ values at which Ba/O-terminated surface dominate. In addition, the availability of Ba dramatically stabilizes (1 1 2) facets. It should be noted that while significant amounts of bare W (1 1 2) is stable at low temperatures, as noted in discussion about pure W particles, these shapes likely are kinetically constrained, and likely appear as (1 1 0)-terminated particles with (1 1 2)-rounded (1 1 0)/(1 1 0) edges. Of particular importance to cathodes is that (1 1 2) facets require Ba to appear. This shows that both careful control of $O_2$ availability and the presence of Ba can produce (1 1 2) facetting on W nanocrystals.

## 4. Summary and conclusion

We have applied DFT and DFPT calculations to compute bulk reference free energies and surface excess free energies accounting for vibrational and, where appropriate, configurational entropies of solid particles and particle surfaces. We have applied these calculations to a family of bare and decorated crystal surfaces relevant for thermionic cathodes widely applied in vacuum electronics. Using these temperature- and chemical potential-dependent surface free energies, we have constructed particle configuration maps that highlight the shape and surface chemistry of particles at equilibrium over a range of temperatures and environmental conditions (represented by the chemical potential of environmentally available species). Such maps, constructed here for W particles in O- or Ba/O-containing environments, demonstrate the critical role that the availability of Ba plays in controlling both the shape and chemistry of W particle surfaces at application-relevant conditions. In particular, the (1 1 2) facets widely observed in thermionic cathodes are shown to only be present when Ba is available, as these facets are not appreciably expressed on W particles in O-only environments. These findings highlight the broad power of DFT+DFPT computed particle configuration maps: revealing connections between and insight into particle behavior and properties as a function of experimentally-relevant conditions.

## CRediT authorship contribution statement

**Mujan N. Seif:** Conceptualization, Methodology, Software, Validation, Formal analysis, Investigation, Resources, Data curation, Writing - original draft, Writing - review & editing, Visualization. **Matthew J. Beck:** Conceptualization, Methodology, Validation, Resources, Data curation, Writing - review & editing, Visualization, Supervision, Project administration, Funding acquisition.

## Declaration of Competing Interest

The authors declare that they have no known competing financial interests or personal relationships that could have appeared to influence the work reported in this paper.

## Acknowledgments

This work was financially supported by the Defense Advanced Research Projects Agency (DARPA) Innovative Vacuum Electronics Science and Technology (INVEST) program, under Grant No. N66001-16-1-4041. The views, opinions, and/or findings expressed are those of the author(s) and should not be interpreted as representing the official views or policies of the Department of Defense or the U.S. Government.

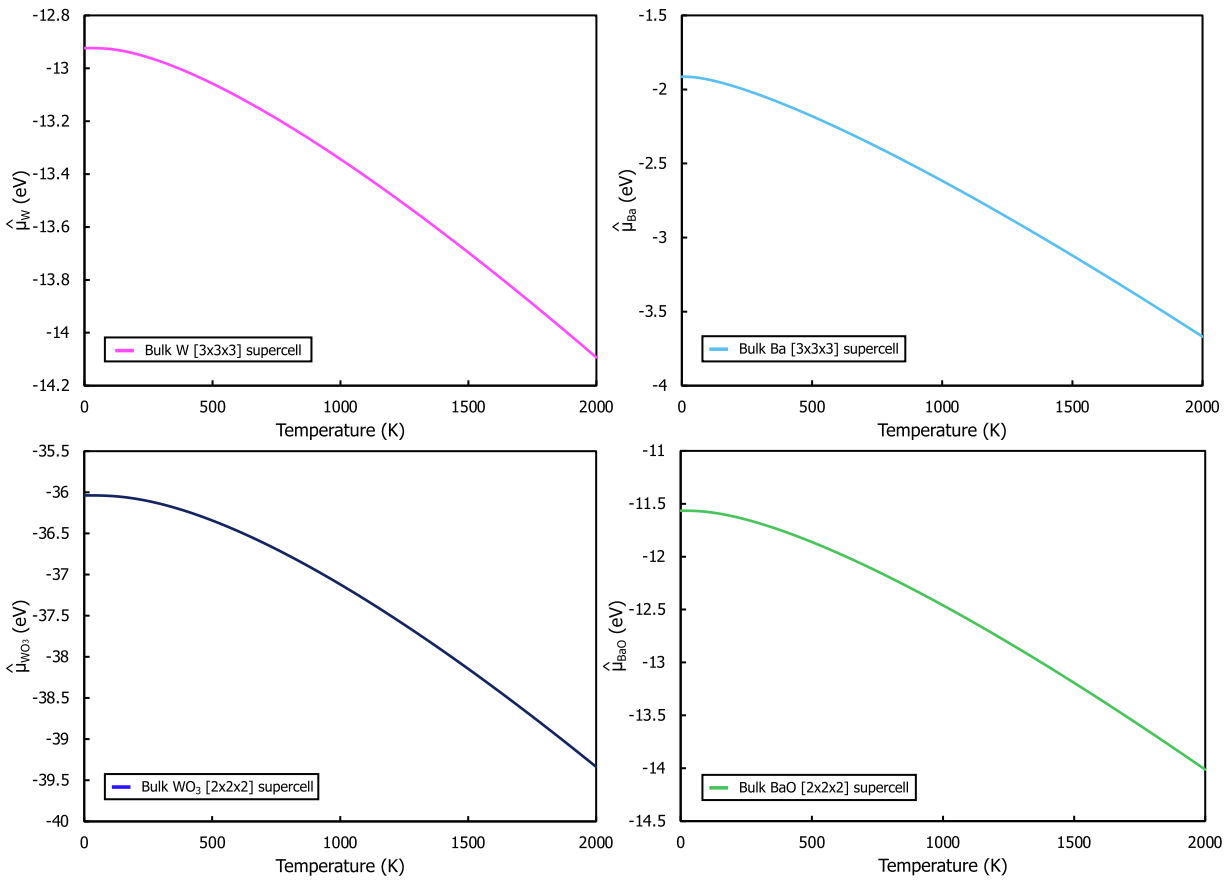


**Fig. 7.** Bulk $\widehat{\mu}$ values for (a) W, (b) Ba, (c) $WO_3$, and (d) BaO, each from 0–2000 K.

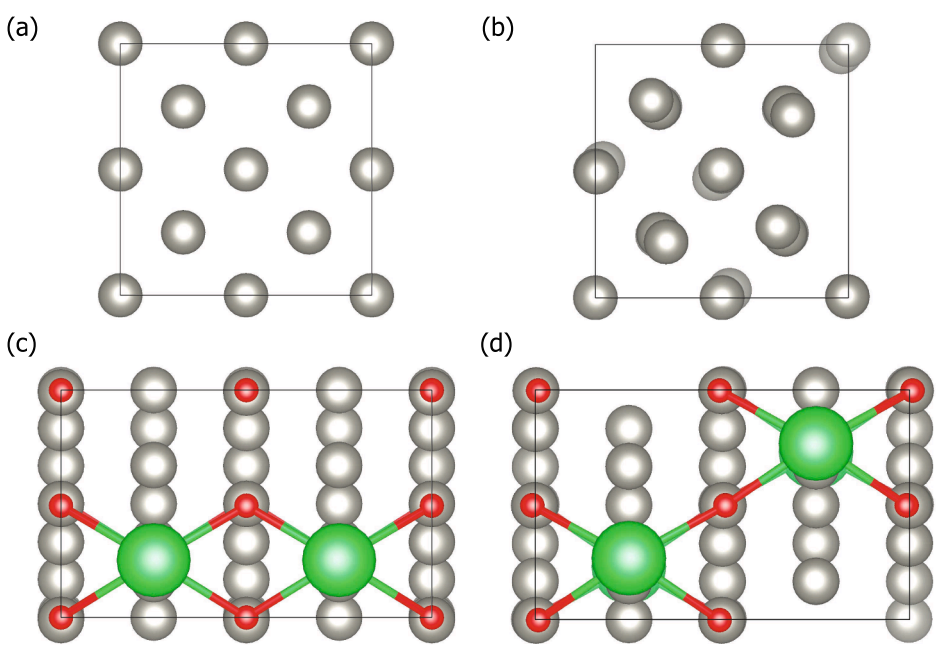


**Fig. 8.** (top) The bare W (0 0 1) surface with (a) an ideal termination and (b) the lower energy reconstruction. (bottom) The $Ba_{0.50}O$-*top*/W(1 1 2) [2 × 2] with Ba atoms in a (a) "row" pattern and a (b) "zig-zag" pattern. (W atoms are gray, O atoms are red, Ba atoms are green). (For interpretation of the references to color in this figure legend, the reader is referred to the web version of this article.)

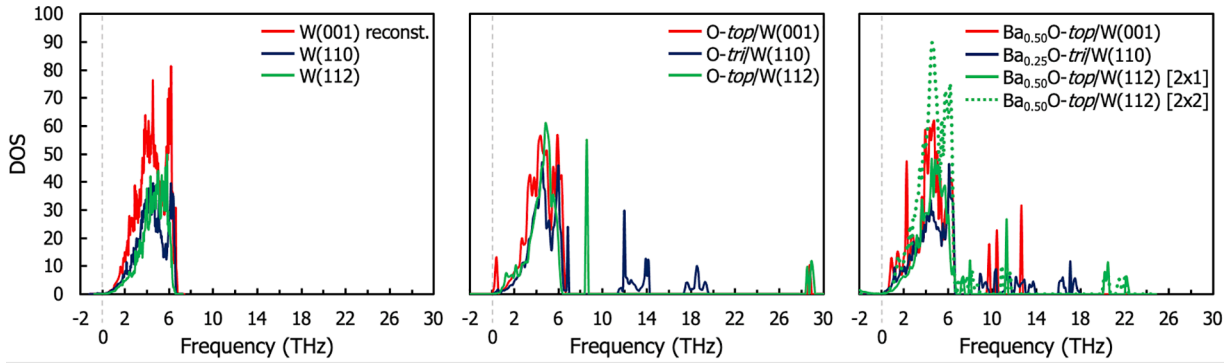


**Fig. 9.** Phonon density of states for each of the surfaces examined here.

## Appendix A

### A.1. Bulk free energies

Fig. 7 reports computed bulk free energies ($\widehat{\mu}_i$) for W, Ba, $WO_3$, and BaO. Bulk free energies of W ($\widehat{\mu}_W$) are computed as described in earlier text. Bulk free energies of Ba ($\widehat{\mu}_{Ba}$) is computed for a body-centered cubic structure (mp-122 on The Materials Project [82]), and of BaO ($\widehat{\mu}_{BaO}$) for a cubic structure (mp-1342 on The Materials Project [82]). In the case of $\widehat{\mu}_{WO_3}$, the equilibrium phase is known to vary with temperature. Here we have chosen the tetragonal phase (mp-19443 on The Materials Project [82]), expected to be stable at temperatures above ~1000 K [86], as the reference phase.

### A.2. Surface pDOS and Structures

Fig. 8 shows the bare W (0 0 1) with both the ideal-termination as well as the lower energy reconstruction, as well as the two $Ba_{0.50}$O-*top*/W(1 1 2) surface configurations discussed in earlier text. Fig. 9 includes the phonon density of states for each of the surfaces evaluated in this investigation.

## References


[1] S. Wang, W. Lu, O. Tovmachenko, U.S. Rai, H. Yu, P.C. Ray, Challenge in understanding size and shape dependent toxicity of gold nanomaterials in human skin keratinocytes, Chem. Phys. Lett. 463 (1–3) (2008) 145–149, https://doi.org/10.1016/j.cplett.2008.08.039.

[2] R.A. Yokel, M.T. Tseng, M. Dan, J.M. Unrine, U.M. Graham, P. Wu, E.A. Grulke, Biodistribution and biopersistence of ceria engineered nanomaterials: Size dependence, Nanomed. Nanotechnol. Biol. Med. 9 (3) (2013) 398–407, https://doi.org/10.1016/j.nano.2012.08.002.

[3] E. Blanco, A. Hsiao, A.P. Mann, M.G. Landry, F. Meric-Bernstam, M. Ferrari, Nanomedicine in cancer therapy: Innovative trends and prospects, Cancer Sci. 102 (7) (2011) 1247–1252, https://doi.org/10.1111/j.1349-7006.2011.01941.x.

[4] M. Estanqueiro, M.H. Amaral, J. Conceição, J.M. Sousa Lobo, Nanotechnological carriers for cancer chemotherapy: The state of the art, Colloids Surfaces. B, Biointerfaces 126 (2015) 631–648, https://doi.org/10.1016/j.colsurfb.2014.12.041.

[5] E. Pérez-Herrero, A. Fernández-Medarde, Advanced targeted therapies in cancer: Drug nanocarriers, the future of chemotherapy, 0, Eur. J. Pharmaceutics Biopharmaceutics: Off. J. Arbeitsgemeinschaft Fur Pharmazeutische Verfahrenstechnik e.V 93 (2015) 52–79, https://doi.org/10.1016/j.ejpb.2015.03.018.

[6] Y. Zhu, L. Liao, Applications of nanoparticles for anticancer drug delivery: a review, J. Nanosci. Nanotechnol. 15 (7) (2015) 4753–4773, https://doi.org/10.1166/jnn.2015.10298.

[7] S. Sultana, M.R. Khan, M. Kumar, S. Kumar, M. Ali, Nanoparticles-mediated drug delivery approaches for cancer targeting: A review, J. Drug Target. 21 (2) (2013) 107–125, https://doi.org/10.3109/1061186X.2012.712130.

[8] R.A. Yokel, J.M. Unrine, P. Wu, B. Wang, E.A. Grulke, Nanoceria biodistribution and retention in the rat after its intravenous administration are not greatly influenced by dosing schedule, dose, or particle shape, Environ. Sci. Nano 1 (6) (2014) 549–560, https://doi.org/10.1039/C4EN00035H.

[9] B. Wang, P. Wu, R.A. Yokel, E.A. Grulke, Influence of surface charge on lysozyme adsorption to ceria nanoparticles, Appl. Surf. Sci. 258 (14) (2012) 5332–5341, https://doi.org/10.1016/j.apsusc.2012.01.142.

[10] G.D. Barmparis, Z. Lodziana, N. Lopez, I.N. Remediakis, Nanoparticle shapes by using Wulff constructions and first-principles calculations, Beilstein J. Nanotechnol. 6 (2015) 361–368, https://doi.org/10.3762/bjnano.6.35.

[11] J.E. Mondloch, E. Bayram, R.G. Finke, A review of the kinetics and mechanisms of formation of supported-nanoparticle heterogeneous catalysts, J. Mol. Catal. A: Chem. 355 (2012) 1–38, https://doi.org/10.1016/j.molcata.2011.11.011.

[12] J.B. Sambur, P. Chen, Approaches to single-nanoparticle catalysis, Annu. Rev. Phys. Chem. 65 (1) (2014) 395–422, https://doi.org/10.1146/annurev-physchem-040513-103729.

[13] F. Raimondi, G.G. Scherer, R. Kötz, A. Wokaun, Nanoparticles in energy technology: examples from electrochemistry and catalysis, Angew. Chem. Int. Ed. 44 (15) (2005) 2190–2209, https://doi.org/10.1002/anie.200460466.

[14] J.D. Aiken, R.G. Finke, A review of modern transition-metal nanoclusters: Their synthesis, characterization, and applications in catalysis, J. Mol. Catal. A: Chem. 145 (1) (1999) 1–44, https://doi.org/10.1016/S1381-1169(99)00098-9.

[15] E.L. Lim, C.C. Yap, M.A. Mat Teridi, C.H. Teh, A.R. bin Mohd Yusoff, M.H. Hj Jumali, A review of recent plasmonic nanoparticles incorporated P3HT: PCBM organic thin film solar cells, Org. Electron. 36 (2016) 12–28, https://doi.org/10.1016/j.orgel.2016.05.029.

[16] S. Magdassi, M. Grouchko, A. Kamyshny, Copper nanoparticles for printed electronics: routes towards achieving oxidation stability, Materials 3 (9) (2010) 4626–4638, https://doi.org/10.3390/ma3094626.

[17] Y. Lee, J.-R. Choi, K.J. Lee, N.E. Stott, D. Kim, Large-scale synthesis of copper nanoparticles by chemically controlled reduction for applications of inkjet-printed electronics, Nanotechnology 19 (41) (2008) 415604, https://doi.org/10.1088/0957-4484/19/41/415604.

[18] S. Mallakpour, M. Madani, A review of current coupling agents for modification of metal oxide nanoparticles, Prog. Org. Coat. 86 (2015) 194–207, https://doi.org/10.1016/j.porgcoat.2015.05.023.

[19] J.W. Boley, E.L. White, R.K. Kramer, Mechanically sintered gallium-indium nanoparticles, Adv. Mater. 27 (14) (2015) 2355–2360, https://doi.org/10.1002/adma.201404790.

[20] A. Shavel, L.M. Liz-Marzán, Shape control of iron oxide nanoparticles, PCCP 11 (19) (2009) 3762–3766, https://doi.org/10.1039/B822733K.

[21] M.H. Magnusson, K. Deppert, J.-O. Malm, J.-O. Bovin, L. Samuelson, Gold nanoparticles: production, reshaping, and thermal charging, J. Nanopart. Res. 1 (2) (1999) 243–251, https://doi.org/10.1023/A:1010012802415.

[22] L.D. Marks, L. Peng, Nanoparticle shape, thermodynamics and kinetics, J. Phys.: Condens. Matter 28 (5) (2016) 053001, https://doi.org/10.1088/0953-8984/28/5/053001.

[23] M. Naito, T. Yokoyama, K. Hosokawa, K. Nogi, Nanoparticle Technology Handbook, Elsevier, 2018.

[24] W.J. Kennedy, S. Izor, B.D. Anderson, G. Frank, V. Varshney, G.J. Ehlert, Thermal reshaping dynamics of gold nanorods: influence of size, shape, and local environment, ACS Appl. Mater. Interfaces 10 (50) (2018) 43865–43873, https://doi.org/10.1021/acsami.8b12965.

[25] N. Combe, P. Jensen, A. Pimpinelli, Changing shapes in the nanoworld, Phys. Rev. Lett. 85 (1) (2000) 110–113, https://doi.org/10.1103/PhysRevLett.85.110.

[26] W. Gao, Y. Hou, Z.D. Hood, X. Wang, K. More, R. Wu, Y. Xia, X. Pan, M. Chi, Direct in situ observation and analysis of the formation of palladium nanocrystals with high-index facets, Nano Lett. 18 (11) (2018) 7004–7013, https://doi.org/10.1021/acs.nanolett.8b02953.

[27] X. Liu, Q. Zhou, T.L. Maxwell, B. Vancil, M.J. Beck, T.J. Balk, Scandate cathode surface characterization: emission testing, elemental analysis and morphological

evaluation, Mater. Charact. 148 (2019) 188–200, https://doi.org/10.1016/j.matchar.2018.12.013.
[28] S. Yamamoto, Fundamental physics of vacuum electron sources, Rep. Prog. Phys. 69 (1) (2006) 181–232, https://doi.org/10.1088/0034-4885/69/1/R04.
[29] G. Gaertner, P. Geittner, D. Raasch, Low temperature and cold emission of scandate cathodes, Appl. Surf. Sci. 201 (1–4) (2002) 61–68, https://doi.org/10.1016/S0169-4332(02)00501-9.
[30] G. Gaertner, D. Barratt, Life-limiting mechanisms in Ba-oxide, Ba-dispenser and Ba-Scandate cathodes, Appl. Surf. Sci. 251 (1–4) (2005) 73–79, https://doi.org/10.1016/j.apsusc.2005.03.213.
[31] Q. Zhou, X. Liu, T. Maxwell, B. Vancil, T.J. Balk, M.J. Beck, BaxScyOz on W (0 0 1), (1 1 0), and (1 1 2) in scandate cathodes: Connecting to experiment via mu_o and equilibrium crystal shape, Appl. Surf. Sci. 458 (2018) 827–838, https://doi.org/10.1016/j.apsusc.2018.07.060.
[32] A.E. Kandjani, M.F. Tabriz, B. Pourabbas, Sonochemical synthesis of ZnO nanoparticles: The effect of temperature and sonication power, Mater. Res. Bull. 43 (3) (2008) 645–654, https://doi.org/10.1016/j.materresbull.2007.04.005.
[33] M.B. Kasture, P. Patel, A.A. Prabhune, C.V. Ramana, A.A. Kulkarni, B.L.V. Prasad, Synthesis of silver nanoparticles by sophorolipids: Effect of temperature and sophorolipid structure on the size of particles, J. Chem. Sci. 120 (6) (2008) 515–520, https://doi.org/10.1007/s12039-008-0080-6.
[34] M. Mazaheri, A.M. Zahedi, S.K. Sadrnezhaad, Two-step sintering of nanocrystalline ZnO compacts: effect of temperature on densification and grain growth, J. Am. Ceram. Soc. 91 (1) (2008) 56–63, https://doi.org/10.1111/j.1551-2916.2007.02029.x.
[35] B. Dikici, M. Gavgali, F. Bedir, Synthesis of in situ TiC nanoparticles in liquid aluminum: The effect of sintering temperature, J. Compos. Mater. 45 (8) (2011) 895–900, https://doi.org/10.1177/0021998310377939.
[36] S.E. Shirsath, R.H. Kadam, A.S. Gaikwad, A. Ghasemi, A. Morisako, Effect of sintering temperature and the particle size on the structural and magnetic properties of nanocrystalline Li0.5Fe2.5O4, J. Magn. Magn. Mater. 323 (23) (2011) 3104–3108, https://doi.org/10.1016/j.jmmm.2011.06.065.
[37] M. Ardestani, H.R. Rezaie, H. Arabi, H. Razavizadeh, The effect of sintering temperature on densification of nanoscale dispersed W–20–40%wt Cu composite powders, Int. J. Refract. Met. Hard Mater. 27 (5) (2009) 862–867, https://doi.org/10.1016/j.ijrmhm.2009.04.004.
[38] L. Zhang, R. He, H.-C. Gu, Synthesis and kinetic shape and size evolution of magnetite nanoparticles, Mater. Res. Bull. 41 (2) (2006) 260–267, https://doi.org/10.1016/j.materresbull.2005.08.024.
[39] H. Yoshida, K. Matsuura, Y. Kuwauchi, H. Kohno, S. Shimada, M. Haruta, S. Takeda, Temperature-dependent change in shape of platinum nanoparticles supported on CeO2 during catalytic reactions, Appl. Phys. Express 4 (6) (2011) 065001, https://doi.org/10.1143/APEX.4.065001.
[40] B. Zhu, J. Meng, Y. Gao, Equilibrium shape of metal nanoparticles under reactive gas conditions, J. Phys. Chem. C 121 (10) (2017) 5629–5634, https://doi.org/10.1021/acs.jpcc.6b13021.
[41] F. Tao, S. Dag, L.-W. Wang, Z. Liu, D.R. Butcher, M. Salmeron, G.A. Somorjai, Restructuring of hex-Pt(100) under CO Gas environments: formation of 2-D nanoclusters, Nano Lett. 9 (5) (2009) 2167–2171, https://doi.org/10.1021/nl900809u.
[42] Y. Jiang, H. Li, Z. Wu, W. Ye, H. Zhang, Y. Wang, C. Sun, Z. Zhang, In situ observation of hydrogen-induced surface faceting for palladium-copper nanocrystals at atmospheric pressure, Angew. Chem. Int. Ed. 55 (40) (2016) 12427–12430, https://doi.org/10.1002/anie.201605956.
[43] G.D. Barmparis, I.N. Remediakis, Dependence on CO adsorption of the shapes of multifaceted gold nanoparticles: A density functional theory, Phys. Rev. B 86 (8) (2012) 085457, https://doi.org/10.1103/PhysRevB.86.085457.
[44] B. Zhu, Z. Xu, C. Wang, Y. Gao, Shape evolution of metal nanoparticles in water vapor environment, Nano Lett. 16 (4) (2016) 2628–2632, https://doi.org/10.1021/acs.nanolett.6b00254.
[45] X. Tian, T. Wang, L. Fan, Y. Wang, H. Lu, Y. Mu, A DFT based method for calculating the surface energies of asymmetric MoP facets, Appl. Surf. Sci. 427 (2018) 357–362, https://doi.org/10.1016/j.apsusc.2017.08.172.
[46] Y.-J.-Z. Xu, J.-X. Shang, F.-H. Wang, First-principles study of electronic properties and stability of Nb 5 SiB 2 (0 0 1) surface, Chin. Phys. B 20 (3) (2011) 037101, https://doi.org/10.1088/1674-1056/20/3/037101.
[47] H. Graoui, S. Giorgio, C. Henry, Shape variations of Pd particles under oxygen adsorption, Surf. Sci. 417 (2–3) (1998) 350–360, https://doi.org/10.1016/S0039-6028(98)00688-8.
[48] H. Wang, C. Xie, The effects of oxygen partial pressure on the microstructures and photocatalytic property of ZnO nanoparticles, Physica E 40 (8) (2008) 2724–2729, https://doi.org/10.1016/j.physe.2007.12.012.
[49] M. Zysler, D. Zitoun, Octahedral to cuboctahedral shape transition in 6 nm Pt3Ni nanocrystals for oxygen reduction reaction electrocatalysis, Particle Particle Syst. Characteriz. 37 (4) (2020) 2000002, https://doi.org/10.1002/ppsc.202000002.
[50] S. Sun, J. Zhu, S. Gu, X. Li, W. Lei, Y. Jiang, D. Yi, G. Chen, First principles investigation of the surface stability and equilibrium morphology of MoO3, Appl. Surf. Sci. 467–468 (2019) 753–759, https://doi.org/10.1016/j.apsusc.2018.10.162.
[51] L. Zhu, K.L. Yao, Z.L. Liu, First-principles study of the polar (111) surface of Fe3O4, Phys. Rev. B 74(3). doi: 10.1103/PhysRevB.74.035409.
[52] S.M. Souvi, M. Badawi, J.-F. Paul, S. Cristol, L. Cantrel, A DFT study of the hematite surface state in the presence of H2, H2O and O2, Surf. Sci. 610 (2013) 7–15, https://doi.org/10.1016/j.susc.2012.12.012.
[53] J. Noh, O.I. Osman, S.G. Aziz, P. Winget, J.-L. Brédas, Magnetite Fe3O4 (111) surfaces: impact of defects on structure, stability, and electronic properties, Chem. Mater. 27 (17) (2015) 5856–5867, https://doi.org/10.1021/acs.chemmater.5b02885.
[54] N.C. Wilson, S.P. Russo, Ilmenite (0001) surface investigated using hybrid density functional theory, Phys. Rev. B 84(7). doi:10.1103/PhysRevB.84.075310.
[55] A. Barbier, A. Stierle, F. Finocchi, J. Jupille, Stability and stoichiometry of (polar) oxide surfaces for varying oxygen chemical potential, J. Phys.: Condens. Matter 20 (18) (2008) 184014, https://doi.org/10.1088/0953-8984/20/18/184014.
[56] N. Wilson, Investigation of hybrid density functional theory in the calculation of the structure and properties of transition metal oxides, P.D., RMIT, Melbourne, AUS, 2009.
[57] Y. Meng, X.-W. Liu, M. Bai, W.-P. Guo, D.-B. Cao, Y. Yang, Y.-W. Li, X.-D. Wen, Prediction on morphologies and phase equilibrium diagram of iron oxides nanoparticles, Appl. Surf. Sci. 480 (2019) 478–486, https://doi.org/10.1016/j.apsusc.2019.03.005.
[58] C.A. Ponce, M.A. Caravaca, R.A. Casali, Ab initio studies of structure, electronic properties, and relative stability of SnO2 nanoparticles as a function of stoichiometry, temperature, and oxygen partial pressure, J. Phys. Chem. C 119 (27) (2015) 15604–15617, https://doi.org/10.1021/jp512343q.
[59] F. Mittendorfer, N. Seriani, O. Dubay, G. Kresse, Morphology of mesoscopic Rh and Pd nanoparticles under oxidizing conditions, Phys. Rev. B 76(23). doi: 10.1103/PhysRevB.76.233413.
[60] M.W. Chase, J.L. Curnutt, A.T. Hu, H. Prophet, A.N. Syverud, L.C. Walker, JANAF thermochemical tables, 1974 supplement, J. Phys. Chem. Ref. Data 1974 (1974) 171.
[61] E. Mohammadpour, M. Altarawneh, Z.-T. Jiang, N. Mondinos, B.Z. Dlugogorski, Electronic properties and stability phase diagrams for cubic BN surfaces, Mol. Simul. 43 (4) (2017) 267–275, https://doi.org/10.1080/08927022.2016.1262953.
[62] Y. Zhang, S. Sanvito, First-principles investigation of the thermodynamic stability of MB2 materials surfaces (M = Ti/Zr/Hf), J. Am. Ceram. Soc. 101 (9) (2018) 4118–4127, https://doi.org/10.1111/jace.15547.
[63] A. Togo, I. Tanaka, First principles phonon calculations in materials science, Scripta Mater. 108 (2015) 1–5, https://doi.org/10.1016/j.scriptamat.2015.07.021.
[64] S. Schönecker, X. Li, B. Johansson, S.K. Kwon, L. Vitos, Thermal surface free energy and stress of iron, Sci. Rep. 5 (1) (2015) 14860, https://doi.org/10.1038/srep14860.
[65] S. Baroni, P. Giannozzi, E. Isaev, Density-functional perturbation theory for quasi-harmonic calculations, Rev. Mineral. Geochem. 71 (1) (2010) 39–57, https://doi.org/10.2138/rmg.2010.71.3.
[66] M. Geng, H. Jónsson, Density functional theory calculations and thermodynamic analysis of bridgmanite surface structure, PCCP 21 (3) (2019) 1009–1013, https://doi.org/10.1039/C8CP06702C.
[67] P. Kempisty, Y. Kangawa, Evolution of the free energy of the GaN(0001) surface based on first-principles phonon calculations, Phys. Rev. B 100(8). doi:10.1103/PhysRevB.100.085304.
[68] D. Scheiber, O. Renk, M. Popov, L. Romaner, Temperature dependence of surface and grain boundary energies from first principles, Phys. Rev. B 101 (17) (2020) 174103, https://doi.org/10.1103/PhysRevB.101.174103.
[69] R.V. Zucker, D. Chatain, U. Dahmen, S. Hagège, W.C. Carter, New software tools for the calculation and display of isolated and attached interfacial-energy minimizing particle shapes, J. Mater. Sci. 47 (24) (2012) 8290–8302, https://doi.org/10.1007/s10853-012-6739-x.
[70] B. Fultz, Vibrational thermodynamics of materials, Prog. Mater Sci. 55 (4) (2010) 247–352, https://doi.org/10.1016/j.pmatsci.2009.05.002.
[71] G. Wulff, XXY. Zur Frage der Geschwindigkeit des Wachs- thums und der Auflosung der Krystallflachen, Z. Kristallogr. 34 (1–6) (1901) 82, https://doi.org/10.1524/zkri.1901.34.1.449.
[72] G. Kresse, J. Furthmüller, Efficient iterative schemes for ab initio total-energy calculations using a plane-wave basis set, Phys. Rev. B 54 (16) (1996) 11169–11186, https://doi.org/10.1103/PhysRevB.54.11169.
[73] J.P. Perdew, K. Burke, M. Ernzerhof, Generalized gradient approximation made simple, Phys. Rev. Lett. 77 (18) (1996) 3865–3868, https://doi.org/10.1103/PhysRevLett.77.3865.
[74] P.E. Blöchl, Projector augmented-wave method, Phys. Rev. B 50 (24) (1994) 17953–17979, https://doi.org/10.1103/PhysRevB.50.17953.
[75] D. Singh, S.-H. Wei, H. Krakauer, Instability of the ideal tungsten (0 0 1) surface, Phys. Rev. Lett. 57 (26) (1986) 3292–3295, https://doi.org/10.1103/PhysRevLett.57.3292.
[76] R. Kumar, H.E. Grenga, Surface energy anisotropy of tungsten, Surf. Sci. 59 (2) (1976) 612–618, https://doi.org/10.1016/0039-6028(76)90039-X.
[77] A. Szczepkowicz, A. Ciszewski, Faceting of curved tungsten surface induced by palladium, Surf. Sci. 515 (2–3) (2002) 441–452, https://doi.org/10.1016/S0039-6028(02)01960-X.
[78] T. Acsente, R. Negrea, L. Nistor, E. Matei, C. Grisolia, R. Birjega, G. Dinescu, Tungsten nanoparticles with controlled shape and crystallinity obtained by magnetron sputtering and gas aggregation, Mater. Lett. 200 (2017) 121–124, https://doi.org/10.1016/j.matlet.2017.04.105.
[79] C. Arnas, A. Chami, L. Couëdel, T. Acsente, M. Cabié, T. Neisius, Thermal balance of tungsten monocrystalline nanoparticles in high pressure magnetron discharges, Phys. Plasmas 26 (5) (2019) 053706, https://doi.org/10.1063/1.5095932.
[80] M.H. Magnusson, K. Deppert, J.-O. Malm, Single-crystalline tungsten nanoparticles produced by thermal decomposition of tungsten hexacarbonyl, J. Mater. Res. 15 (7) (2000) 1564–1569, https://doi.org/10.1557/JMR.2000.0224.
[81] J.C. Tracy, J.M. Blakely, A study of facetting of tungsten single crystal surfaces, Surf. Sci. 13 (2) (1969) 313–336, https://doi.org/10.1016/0039-6028(69)90194-0.

[82] A. Jain, S. Ong, G. Hautier, W. Chen, W. Richards, S. Dacek, S. Cholia, D. Gunter, D. Skinner, G. Cedar, K. Persson, The Materials Project: A materials genome approach to accelerating materials innovation, APL Mater. 1(1) (2013). http://doi.org/10.1063/1.4812323.
[83] A.I. Figner, Metal-porous body having pores filled with barium scandate (1967).
[84] M.N. Seif, T.J. Balk, M.J. Beck, Desorption from hot scandate cathodes: effects on vacuum deviceinterior surfaces after long-term operation, Under review: Materials.
[85] M.J. Beck, Computational Materials Science at the University of Kentucky, beckdt.engr.uky.edu.
[86] H.A. Wriedt, The O-W (oxygen-tungsten) system, Bull. Alloy Phase Diagrams 10 (4) (1989) 368–384, https://doi.org/10.1007/BF02877593.